Environmental Science and Pollution Research
https://doi.org/10.1007/s11356-023-28451-7

RESEARCH ARTICLE

Fabrication of ordered layered SnO_2/TiO_2 heterostructures and their photocatalytic performance for methyl blue degradation

Walid Serbout[1] · **Fayçal Bensouici**[2] · **Omar Meglali**[1,3] · **Sabrina Iaiche**[2] · **Mohamed Bououdina**[4] · **Steffano Bellucci**[5] · **Muhammad Humayun**[4]

Received: 7 April 2023 / Accepted: 22 June 2023

Abstract

The rapid growth in population and industrialization has given rise to serious environmental issues, especially the water pollution. Photocatalysis with the assist of semiconductor photocatalysts has been considered as an advanced oxidation technique for degrading a variety of pollutants under solar irradiation. In this work, we have fabricated SnO_2-TiO_2 heterostructures with different ordered layers of SnO_2 and TiO_2 via the sol–gel dip-coating technique and utilized in photocatalysis for degradation of methyl blue dye under UV irradiation. The influence of the layer's position on SnO_2 and TiO_2 properties is investigated via the various techniques. The grazing incidence X-ray diffraction (GIXRD) analysis reveals that the as-prepared films exhibit pure anatase TiO_2 and kesterite SnO_2 phases. The $2SnO_2/2TiO_2$ heterostructure exhibit the maximum crystallite size and smallest deviation from the ideal structure. Scanning electron microscopy cross-section images manifest good adhesion of the layers to each other and to the substrate. Fourier transform infrared spectroscopy reveals the characteristic vibration modes of SnO_2 and TiO_2 phases. UV–visible spectroscopy measurements indicate that all films exhibit high transparency (T = 80%) and the SnO_2 film reveals a direct band gap of 3.6 eV, while the TiO_2 film exhibits an indirect band gap of 2.9 eV. The optimal $2SnO_2/2TiO_2$ heterostructure film revealed best photocatalytic degradation performance and the reaction rate constant for methylene blue solution under UV irradiation. This work will trigger the development of highly efficient heterostructure photocatalysts for environmental remediation.

Keywords Dip-coating · Heterostructure · Ordered layers · Photocatalysis · Methyl blue

Introduction

Global dye production exceeds 7×10^5 t, which is used not only in the textile sector but also in the food, paper, and pharmaceutical industries (Srivastava et al. 2017). It is estimated that about 15% of these dyes are lost during the synthesis, dye processing, dyeing, printing, and finishing processes (Aye et al. 2003). Being common industrial pollutants, the decolorization and mineralization of the dyes via different techniques become necessary. The decomposition of dye molecules may result in the formation of dye fragments, that might be more toxic and environmentally persistent compared to the actual dyes such as aromatic amines. It was reported that conventional physical, chemical, and biological treatment methods for decolorization and decomposition are ineffective, because of their low degradation efficiency, chemical consumption, and high operation costs (Abdel-Messih et al. 2013; Mehrdad and Hashemzadeh 2010). To minimize these limitations,

Responsible Editor: George Z. Kyzas

Muhammad Humayun
mhumayun@psu.edu.sa

[1] Materials Science and Informatics Laboratory, Ziane Achour University, 17000 Djelfa, Algeria

[2] Laboratory of Structures, Properties and Intermolecular Interactions LASPI2A, Department of Matter, Abbes Laghrour University, 40.000 Khenchela, Algeria

[3] Faculty of Sciences, Mohammed Boudiaf University, M'Sila 28000, Algeria

[4] Energy, Water, and Environment Lab, College of Humanities and Sciences, Prince Sultan University, Riyadh 11586, Saudi Arabia

[5] INFN-Laboratori Nazionali Di Frascati, Vie. E. Fermi 54, 00044 Frascati, Italy

photocatalysis received a considerable attention as an innovative treatment technique due to its exceptional capability for environment purification and energy conversion. This technique possesses the potential to oxidize most of the organic pollutants into inorganic minerals such as CO_2 and H_2O (Aplin and Waite 2000; Dai et al. 1996; Pérez et al. 2006; Wang 2007).

Extensive research has been devoted to investigate the photocatalytic performance of different semiconductor photocatalysts including the TiO_2, SnO_2, ZnO, ZrO_2, and CdS (Ferrere et al. 1997; Idota et al. 1997; Minami 2000; Park et al. 2004). Generally, anatase phase TiO_2 has been widely investigated in photocatalysis due to its high activity, low cost, non-toxicity, outstanding chemical stability, and proper conduction band potential (Abd El-Nasser et al. 2020; An et al. 2015; Ashkarran et al. 2015; Dong et al. 2016; Hashimoto et al. 2005; Hoffmann et al. 1995; Pourmadadi et al. 2023). Nevertheless, one of the major disadvantages of TiO_2 is its low quantum efficiency which is caused by the fast recombination rate of electron–hole pairs. In addition, TiO_2 has a large bandgap energy (~ 3.2 eV) and absorb only UV light with $\lambda \leq 387$ nm, which is ca. 4% of the solar spectrum (Dai et al. 1996; Idota et al. 1997; Park et al. 2004). Several approaches have been explored to minimize or avoid these drawbacks in the photocatalytic applications, such as the noble metal deposition and metal/nonmetal oxide doping (Asahi et al. 2001; Bensouici et al. 2017; Benyakhlef et al. 2020; Irie et al. 2003; Ohno et al. 2003). The electron–hole pairs separation in TiO_2 can also be enhanced by doping carbon based nanoparticles (Norouzi et al. 2022). This has broadened the absorption spectra of TiO_2 to some extent, but its photocatalytic activity is still low.

The heterojunction hybrid nanostructure typically consists of two or more semiconductors possess an enhance catalytic performance compared to the single-component catalysts due to their efficient photogenerated charge carrier separation (Gaya and Abdullah 2008; Pal et al. 2022; Qin et al. 2009). Currently, there are various semiconductors that can be used to couple with TiO_2 such as SnO_2, ZnO, Fe_2O_3, CuO, etc., (Lin et al. 2013; Malik et al. 2016; Zhang et al. 2015). Among them, SnO_2 possesses the same crystal symmetry (tetragonal), the molecular units per primitive unit cell ($Z = 2$), and close lattice parameters to that of the TiO_2. Moreover, the valence band edges of SnO_2 and TiO_2 are located at + 4.1 and + 3.1 eV, respectively. While, the conduction band edges of SnO_2 and TiO_2 are located at + 0.5 and − 0.3 eV, respectively. This means that the valence band of TiO_2 is located within the vicinity of SnO_2 band gap (Wang et al. 2009).

Recently, several studies have been reported on the photocatalytic properties of TiO_2/SnO_2 heterostructures (Cheng et al. 2017; de Mendonça et al. 2014; Kawahara et al. 2001; Kusior et al. 2019; Scarisoreanu et al. 2017; Wang et al. 2013; Zakrzewska and Radecka 2007). However, so far, no comparative study has been conducted on the effect of SnO_2 and TiO_2 layer order on the catalytic activity of SnO_2/TiO_2 heterostructures. In this work, TiO_2/SnO_2 heterostructures with different ordered layers of TiO_2 and SnO_2 are grown on glass substrates via the sol–gel dip-coating method using the precursor solutions of tin chloride dihydrate and titanium isopropoxide and explored in photocatalytic degradation of methyl blue dye. Among all of the catalysts, the $2SnO_2/2TiO_2$ heterostructure film revealed superior photocatalytic performance for degradation and reaction rate constant of methylene blue under UV light irradiation. This work will provide a new route for the design and development of cost-effective composite photocatalysts for environmental remediation.

The influence of the layers order on the SnO_2/TiO_2 properties was investigated.

Experimental

Synthesis of SnO_2/TiO_2 heterostructures

Four samples of SnO_2/TiO_2 heterostructures with different order of SnO_2 and TiO_2 layers were prepared using sol–gel dip-coating technique. According to the position of SnO_2 and TiO_2 layers within the heterostructures, the prepared films were named as $2SnO_2/2TiO_2$, $2TiO_2/2SnO_2$, $1SnO_2/1TiO_2$, and $1TiO_2/1SnO_2$ (see Fig. 1). Prior to the deposition of the layers, the soda-lime-glass substrates were

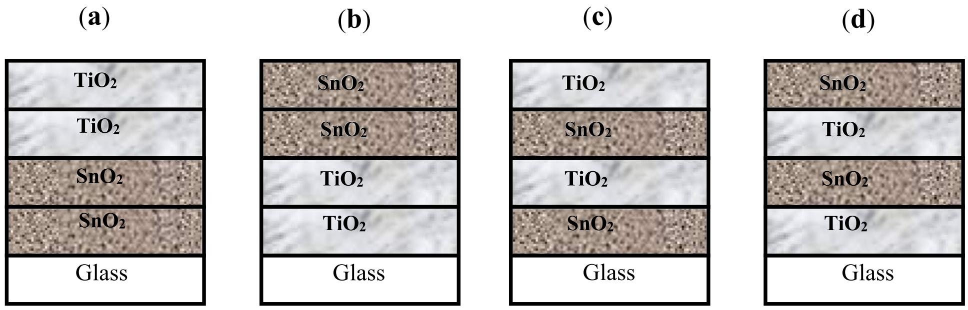

Fig. 1 The position order of the SnO_2 and TiO_2 layers in different heterostructures. **a** Glass/SnO_2/SnO_2/TiO_2/TiO_2 (named $2SnO_2/2TiO_2$). **b** Glass/TiO_2/TiO_2/SnO_2/SnO_2 (named $2TiO_2/2SnO_2$). **c** Glass/SnO_2/TiO_2/SnO_2/TiO_2 (named $1SnO_2/1TiO_2$). **d** Glass/TiO_2/SnO_2/TiO_2/SnO_2 (named $1TiO_2/1SnO_2$)

ultrasonically cleaned with acetone, methanol, and ethanol, and finally washed with distilled water and dried.

For deposition of TiO_2, titanium isopropoxide IV $Ti(OCH_2CH_2CH_3)_4$ (Alfa Aesar 98%, 0.4 M) precursor was dissolved in a solution containing ethanol (Sigma-Aldrich 98%), water, and nitric acid (Sigma-Aldrich 69%). This mixture was then stirred for 1 h (Bensouici et al. 2015). For deposition of SnO_2, 25 mmol of tin chloride dihydrate precursor ($SnCl_2 \cdot 2H_2O$) (Sigma-Aldrich 99%) was dissolved in 100 mL ethanol followed by magnetic stirring at 80 °C for 2 h. The as-deposited TiO_2/SnO_2 heterostructures were then subsequently annealed at 500 °C for 2 h under air environment (Haouanoh et al. 2019).

Characterization

The film's thickness was determined from the cross-section SEM images recorded by scanning electron microscope (SEM) Zeiss Evo 40 SE Detector. The structure of the films was evaluated by means of X-ray diffraction at grazing incidence (GIXRD) using a coupled θ-2θ X-ray diffractometer (XRD) X'PERT PANALYTICAL in the range 10–90° and equipped with monochromatic CuKα_1 radiation of wavelength ($\lambda = 1.54056$ Å). The FTIR spectra were recorded in transmission mode using a Perkin-Elmer Frontier FTIR spectrometer with a resolution of 4 cm^{-1}. The samples pellets for FTIR measurement were prepared by grinding the film scraped from the glass substrate with 1 wt.% KBr. The transmission spectra were recorded at room temperature in the wavelength range 200–1100 nm using Shimadzu spectrophotometer model UV-3100PC.

Photoactivity measurement

The photoactivity of TiO_2/SnO_2 heterostructures was evaluated by measuring the photodegradation of methylene blue (MB) solution under UV irradiation. The four samples were immersed in a volume of 35 mL of MB ($C = 2.5\ 10^{-5}$ mol/L) solution at room temperature and irradiated by a Philips germicidal lamp (G15T8/15W), which was fixed at a distance of 7 cm above the beaker containing the MB solution. The concentration of the dye was measured at its characteristic absorption wavelength of 254 nm.

Results and discussion

X-ray diffraction analysis

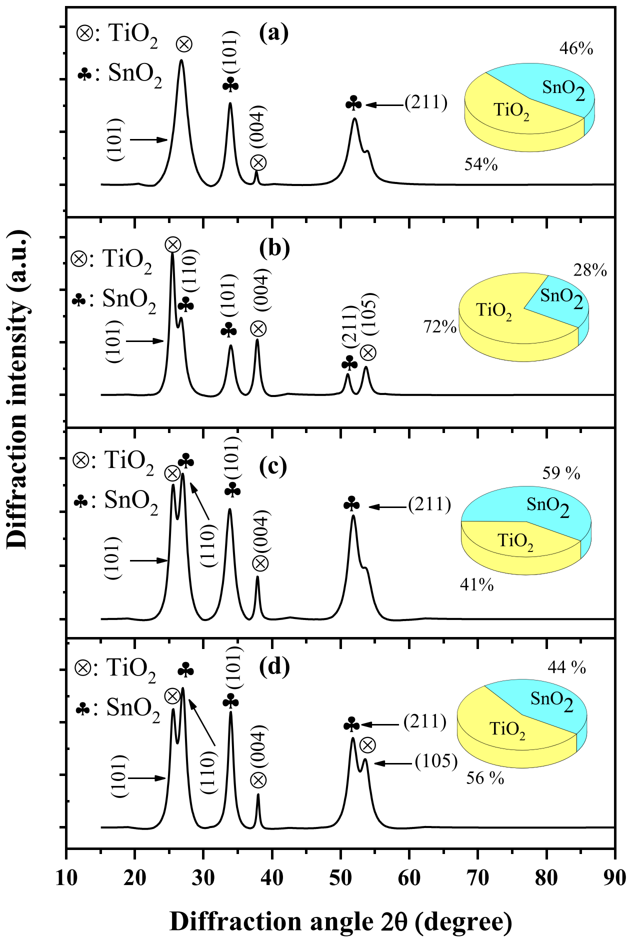

Fig. 2 X-ray diffraction diagramms of synthetized heterostructure for differents order of SnO_2 and TiO_2 layers. **a** $2TiO_2/2SnO_2$, **b** $2SnO_2/2TiO_2$, **c** $1TiO_2/1SnO_2$, **d** $1SnO_2/1TiO_2$. The inserts show the phases quantification calculated by the HighScore software

Figure 2 depicts the evolution of X-ray diffraction patterns of the multilayered thin films grown using different order of TiO_2 and SnO_2, whereas the inset shows the phase quantification determined by HighScore software. All XRD patterns reveal characteristic lines of both TiO_2 and SnO_2 phases. The three peaks located at $2\theta \approx 25.36°$, 37.90°, and 53.95° correspond to (101), (004), and (105) planes of the tetragonal TiO_2 anatase phase whereas the remaining lines located at $2\theta \approx 26.62°$, 33.90°, and 51.8° correspond to (110), (101), and (211) planes of the tetragonal SnO_2 cassiterite phase, which is in good agreement with the JCPDS cards No. 01–073-1764 and No. 01–070-4177, respectively. No additional diffraction peaks assigned to secondary phases are observed, indicating that the prepared films exhibit pure anatase TiO_2 and cassiterite SnO_2 phases.

Both SnO_2 and TiO_2 oxides have a tetragonal crystal system and for this type of structure, the interplanar distance d_{hkl} is estimated by (Eq. 1):

$$d_{hkl} = \frac{a}{\sqrt{h^2 + k^2 + \frac{a^2}{c^2} l^2}} \tag{1}$$

where *a* and *c* d_{hkl} are the lattice constants of the crystal lattice.

The average crystallite size *D* was estimated using the well-known Scherr's formula (Sharma et al. 2012):

$$D = \frac{0.9\ \lambda}{\beta \cos \theta} \tag{2}$$

where β and θ (in radian) are respectively the normalized full width at half maximum and the position of the main peak of the X-ray diffraction pattern.

The dislocation density δ and the microstrain ε have been calculated by Eqs. 3 and 4 (Mathews et al. 2009; Sharma et al. 2012):

$$\delta = \frac{1}{D_s^2} \tag{3}$$

$$\varepsilon = \left(\frac{1}{4}\right) \beta\ \cos\ \theta \tag{4}$$

Based on the abovementioned equations, the structural and microstructural parameters are calculated, and the results are summarized in Table 1. The obtained values are in good agreement with those reported in the JCPDS files and with the results reported in literature for TiO_2 and SnO_2, respectively (Kiruthiga et al. 2022; Sofyan et al. 2018). It is also found that the calculated lattice parameters as well as the microstructural parameters are not strongly affected by the order of SnO_2/TiO_2 or TiO_2/SnO_2 layers. Besides, it can be noticed that the $2SnO_2/2TiO_2$ multilayer has large crystallite size (of both layers) alongside the lowest dislocation densities and micro strain.

Furthermore, it is observed that the ratio $\left(\delta = \frac{c}{a}\right)$ obtained from Table 1, i.e., 0.672 and 2.51 for SnO_2 and TiO_2 structures, is very close to the ideal the stoichiometric coefficient. This indicates that the film with $2SnO_2/2TiO_2$ multilayer shows the smallest deviation from the ideal structure.

The calculation of phase composition is found to varies as follows:

$2TiO_2/2SnO_2$ and $1SnO_2/1TiO_2$ films with 55/45 percentage ratio, whereas $2SnO_2/2TiO_2$ is highly TiO_2-rich (72%) and $1TiO_2/1SnO_2$ is relatively SnO_2-rich (59%). This fluctuation in the TiO_2/SnO_2 ratio may originate from the number and order of layers: 1 or 2 layers and the molecular weight (for TiO_2 and for SnO_2). Furthermore, after the deposition of SnO_2 over TiO_2 film, we observed a peak at 26.62° which might be related to the epitaxial growth of tetragonal cassiterite phase of SnO_2 on the tetragonal anatase phase of TiO_2. This is because, the lattice parameters of anatase TiO_2 and cassiterite SnO_2 are very close to each other, which confirms good adhesion of the thin layers.

SEM observations

From the cross-sectional images (Fig. 3a–d), it can be seen that the interface between the layers and the substrate is homogeneous and has no voids, indicating the good adhesion between the layers and the substrate. The estimated thickness of the different layers is found to vary in a relatively narrow range, i.e., 1.05–1.91 µm and the obtained values are provided in Table 2. The achieved good adhesion between the layers without any microstructural defects besides the relatively homogeneous average thickness will enhance the photocatalytic activity of the as-grown multilayered TiO_2/SnO_2 nanostructures.

FTIR analysis

The FTIR data recorded in the wavenumber range of 400–4000 cm^{-1} is depicted in Fig. 4. The broad lines observed at 3455 and 1636 cm^{-1} are assigned to the bending vibration of absorbed water and surface hydroxyl and O–H stretching mode, respectively (Aziz et al. 2013). The two bands located at 2926 and 2855 cm^{-1} originate from the residual organic traces of

Table 1 The average crystallite size, lattice parameters, microstrain, and dislocation density for differents order of the SnO_2 and TiO_2 layers

Samples	Crystallite size (Å)		Lattice parameters (Å)						Microstrain ($\times 10^{-2}$%)		Dislocation density ($\times 10^{15}$ lines/m^2)	
	TiO_2	SnO_2	TiO_2			SnO_2			TiO_2	SnO_2	TiO_2	SnO_2
			a	c	$\delta = \frac{c}{a}$	*a*	c	$\delta = \frac{c}{a}$				
$2TiO_2/2SnO_2$	143	117	3.747	9.492	2.53	4.665	3.214	0.688	1.09	1.262	4.878	7.235
$2SnO_2/2TiO_2$	181	126	3.769	9.493	2.51	4.699	3.183	0.677	0.87	1.155	3.048	6.235
$1TiO_2/1SnO_2$	124	88	3.729	9.529	2.55	4.705	3.191	0.678	0.16	1.689	6.448	1.273
$1SnO_2/1TiO_2$	136	118	3.750	9.473	2.52	4.662	3.196	0.685	1.15	1.248	5.382	7.079
JCPDS card	/		3.782	9.502	2.51	4.737	3.185	0.672	/			

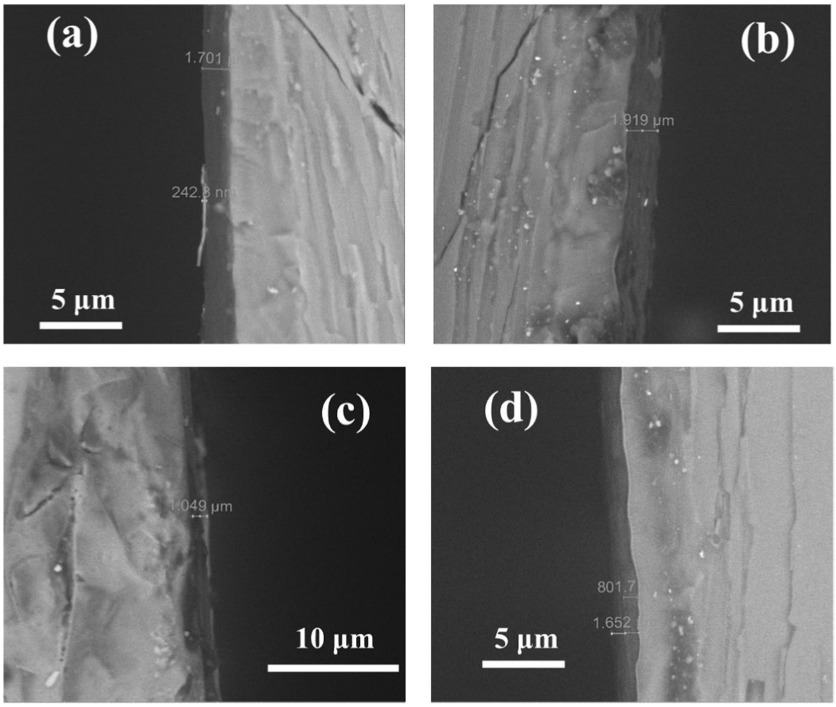

Fig. 3 SEM cross-section images of synthetized multilayer with differents order of SnO_2 and TiO_2 layers. **a** $2SnO_2/2TiO_2$, **b** $2TiO_2/2SnO_2$, **c** $1SnO_2/1TiO_2$, **d** $1TiO_2/1SnO_2$

Table 2 Layer thicknesses, band gap energy of TiO_2 and SnO_2, Urbach energy, and the photocatalytic degradation rate constant K_{app} of fabricated heterostructures for differents order of SnO_2 and TiO_2 layers

Samples	Thickness (µm)	E_g (eV)		E_u (eV)	K_{app} ($\times 10^{-2}$ min^{-1})
		TiO_2	SnO_2		
$2SnO_2/2TiO_2$	1.70	2.94	3.66	0.23	1.13
$1SnO_2/1TiO_2$	1.05	3.02	3.56	0.26	1.11
$2TiO_2/2SnO_2$	1.91	2.94	3.68	0.20	0.92
$1TiO_2/1SnO_2$	1.65	3.14	3.58	0.27	0.71
TiO_2	/	3.2	/	0.14	/
SnO_2	/	/	3.9	0.30	/

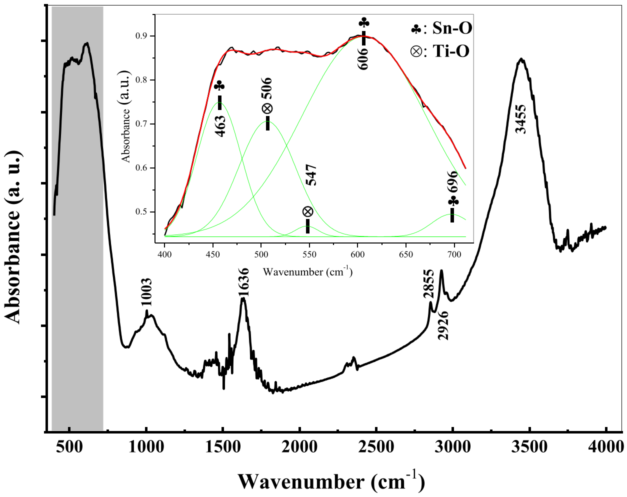

Fig. 4 FTIR spectrum of SnO_2/TiO_2 heterojunction. The green peaks indicate the individual Lorentzian fit of the five lines

organic precursors (Mohammadi et al. 2006). Moreover, the peak centered at 1003 cm^{-1} corresponds to the Si–O vibration mode, which is characteristic of the glass substrate (Yoo et al. 2007).

To identify the oxygen-titanium and oxygen-tin bonds, a new plot representing the absorbance in the region of 400−700 cm^{-1}, is given as inset of Fig. 4. This wide absorbance range is due to the vibrations of both Ti–O and Sn–O bonds of TiO_2 and SnO_2 compounds. The SnO_2 phase manifests three main bands at 463, 606 and 696 cm^{-1}, assigned to the O–Sn–O and Sn–O stretching vibration. Whereas, the Ti–O bond in TiO_2 phase is identified by two sharp bands located at 506 and 547 cm^{-1} (Chetri et al. 2014; Farhadi et al. 2017).

Optical properties

The optical transmittance of the fabricated heterojunction between SnO_2 and TiO_2 layers as a function of irradiation wavelength in the range of 190–1100 nm is illustrated in Fig. 5. Although the general appearance looks identical, the spectra are composed of two regions: (i) the first region for $\lambda < 380$nm (UV region) and is characterized by high absorption (fall of the transmittance) due to the direct electronic transition as well as the movement of electrons from the

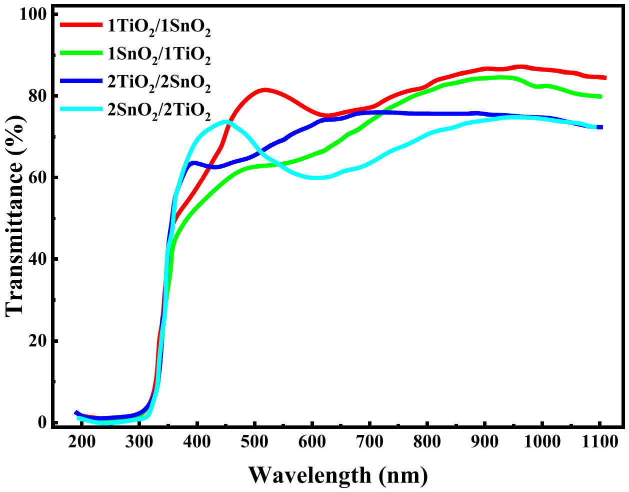

Fig. 5 Transmittance spectra versus wavelength of films prepared with different order of SnO_2 and TiO_2 layers

valence band (VB) to the conduction band (CB) used for the determination of the optical band gap, and (ii) a second region at $\lambda < 380$nm (UV–Vis region) characterized by high transmittance around 75 to 86%.

From the curves shown in Fig. 5, the band gap energy (E_g) and Urbach energy (E_u) are determined according to the well-known energy-exponential relationships defined respectively by (Bensouici et al. 2015; Meglali et al. 2017):

$$(\alpha h\nu)^n = B(h\nu - E_g) \tag{5}$$

$$\alpha = \alpha_0 + \exp(\frac{E}{E_u}) \tag{6}$$

where B and α_0 are constants, $n = 0.5$ or 2 respectively for the indirect band gap (for TiO_2) and direct gap semiconductor transition (for SnO_2), E is the incident photon energy (equals to $h\upsilon$), and α is the absorption coefficient calculated by the following relation (Dakhel 2010):

$$\alpha = -\frac{1}{d}\ln\ T \tag{7}$$

where d is the experimentally estimated film's thickness from the cross-sectional views of the SEM images shown in Fig. 3 (the values are reported in Table 2).

The band gap energy is estimated from the extrapolation of the linear part of $(\alpha h\nu)^{1/2}$ for TiO_2 layer and $(\alpha h\nu)^2$ for SnO_2 (Fig. 6a, b). The expression of the absorption coefficient according to the Urbach's law is expressed by

$$\alpha = \alpha_0 \exp\left(\frac{h\nu}{E_U}\right) \tag{8}$$

where h is Planck's constant, α_0 is a constant, ν is the frequency of absorption, and E_U is Urbach energy. To determine the disorder (Urbach energy) of thin films, we plot the logarithm of α versus of $h\nu$ as mentioned in the following:

$$\ln\alpha = \ln a\alpha_0 + \left(\frac{h\nu}{E_U}\right) \tag{9}$$

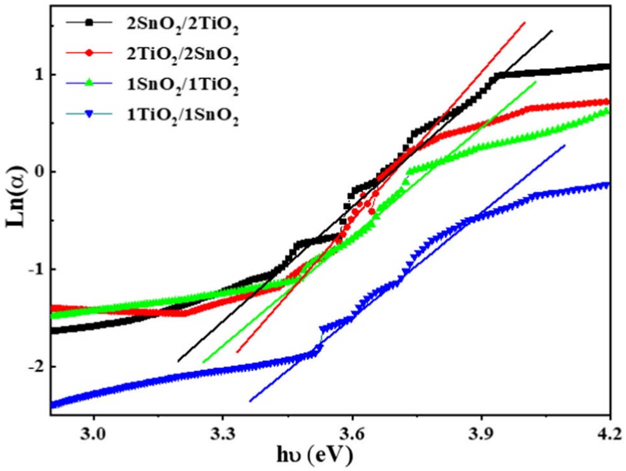

Fig. 7 The plot of ln(α) as a function of photon energy (hν) of films prepared with different order of SnO_2 and TiO_2 layers

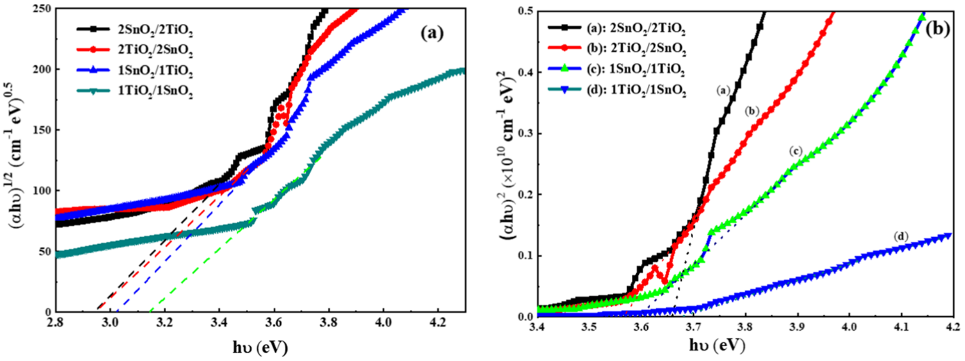

Fig. 6 Tauc plots of **a** TiO_2 (indirect transition) and **b** SnO_2 (direct transition) of films prepared with different order of SnO_2 and TiO_2 layers

Figure 7 shows the plot of (*ln* α) versus ($h\nu$) for all thin multilayer films. Therefore, Urbach energy is determined by the reciprocal slope of the adjusted experimental linear behavior.

The calculated values of band gap energy and Urbach energy are given in Table 2.

It is clearly noted that the change in the optical band gap of the four heterojunctions can be attributed to the mixing of the energy band levels of TiO_2 and SnO_2 semiconductors as well as the layers' order. The energy band gap of TiO_2 and SnO_2 in the heterojunction structures have lower energy band gap values compared to their individual metal oxides (3.2 and 3.9 eV, respectively) (Choudhury and Choudhury 2014; Derrar et al. 2019). The lowering of the band gap energy in the SnO_2/TiO_2 multilayer compared to those of the individual SnO_2 and TiO_2 layer is due to the presence of localized defect states close to the energy bands. The presence of defects leads to an increase in the band tail width ($E_u \approx 0.25$ eV for our multilayer) causes a reduction in energy band gap (Meglali et al. 2014).

Degradation of methylene blue MB

The photodegradation performance of the prepared heterojunctions ($2SnO_2/2TiO_2$, $2TiO_2/2SnO_2$, $1SnO_2/1TiO_2$, and $1TiO_2/1SnO_2$) was examined by the decomposition of 2.5 10^{-5} mol/L of MB solution under UV irradiation at different time intervals. All films were immersed in a volume of 35 mL of MB solution at room temperature and irradiated by a Philips lamp (G15T8/15W, predominant peak at 254 nm), which was fixed at 7 cm above the beakers containing the solutions. The absorbance of methyl blue (MB) solution in the presence of the films exposed at different time interval (from 0 to 4 h with 1-h period) was measured by UV–vis spectrum (Perkin Elmer Lambda EZ 200 type), as shown in Fig. 8a–d.

The photocatalytic degradation rate "D" of the MB solutions for heterojunction films was calculated by the following formula (Eq. 8) (Bensouici et al. 2015).

$$D(\%) = \frac{C_0 - C_t}{C_0} \times 100 \tag{10}$$

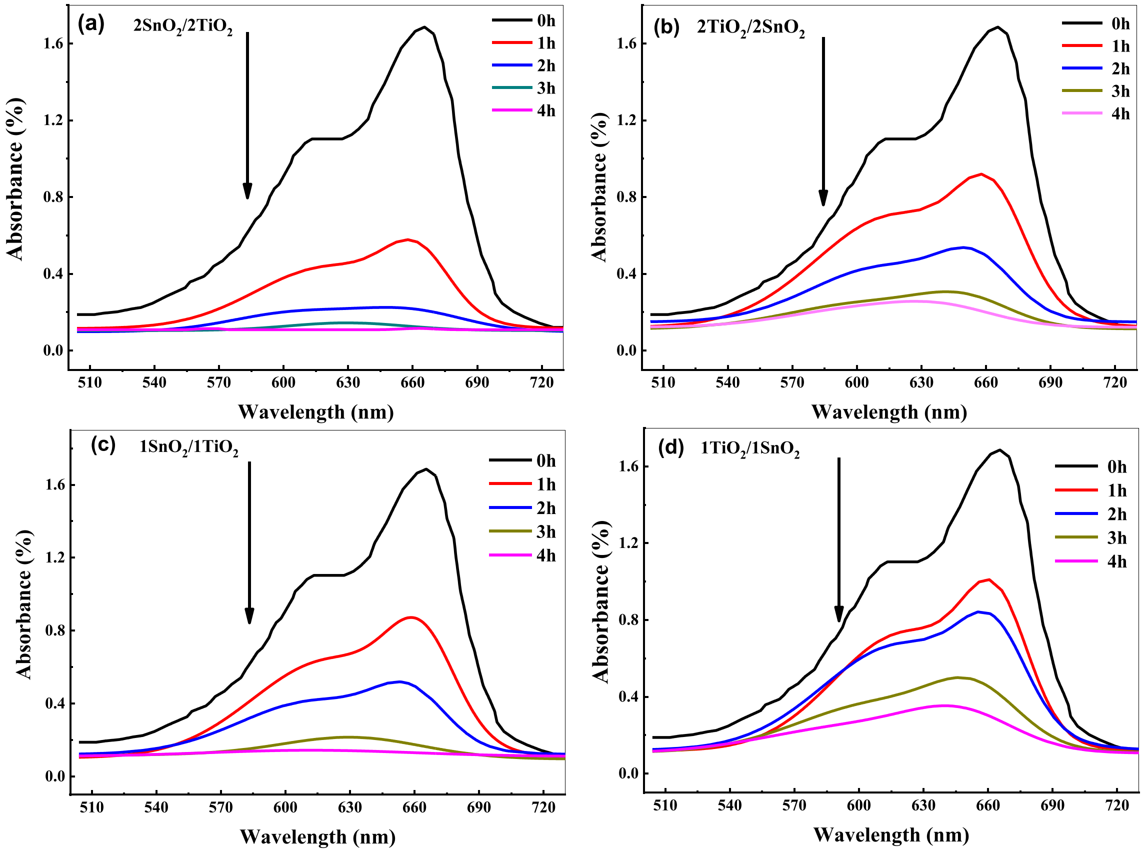

Fig. 8 Optical absorption spectra of the methylene blue dye measured after the photocatalysis process for different exposure times

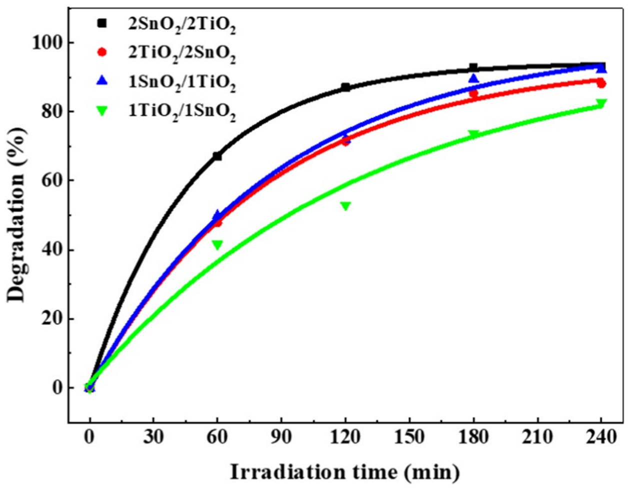

Fig. 9 The photocatalytic degradation efficiency of MB versus the exposure time of films prepared with different order of SnO_2 and TiO_2 layers

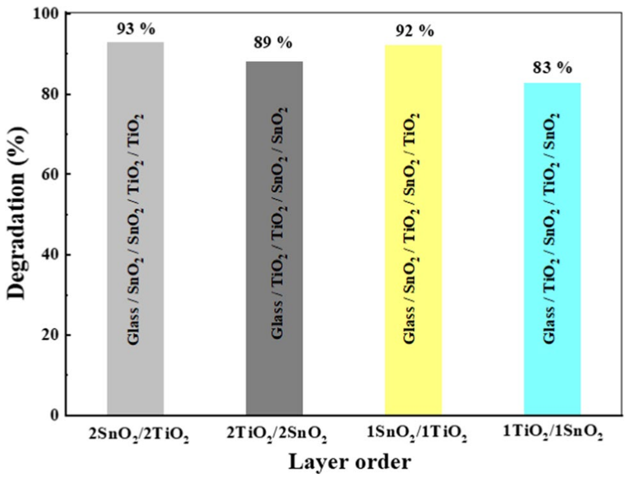

Fig. 10 Degradation of MB histograms in the presence of the different prepared heterojunctions for an exposure time of 180 min

where C_0 is the MB concentration before its exposure to irradiation and C_t is the concentration at a given time t (in minutes) after irradiation. The variation of MB photodegradation rate as a function of irradiation time for the prepared heterojunction films is shown in Fig. 9.

All the prepared heterojunctions display higher photocatalytic activity and degrades the MB progressively during the entire irradiation period with a varying rate. Irrespective the irradiation time, the photocatalytic degradation performance of $2SnO_2/2TiO_2$ film for MB is maximal, i.e., 93%, 92%, 89%, and 83% for $2SnO_2/2TiO_2$, $1SnO_2/1TiO_2$, $2TiO_2/2SnO_2$, and $1TiO_2/1SnO_2$, respectively, after 180 min (Fig. 10). On the other hand, the photocatalytic performance of the samples for MB degradation decreases in the following order of the layers: $2SnO_2/2TiO_2 < 1SnO_2/1TiO_2 < 2TiO_2/2SnO_2 < 1TiO_2/1SnO_2$.

The photocatalytic reaction rate constant k is calculated using to the following pseudo-first-order reaction equation (Fogler 2020):

$$\ln\left(\frac{C_0}{C_t}\right) = K_{app}t \tag{11}$$

where C_0 and C_t are MB dye molar concentration, respectively before and after different irradiation time.

The slope from the plot of $\ln\left(\frac{C_0}{C_t}\right)$ versus the irradiation time gives the value of the photocatalytic reaction rate constant K_{app}. The obtained results are listed in Table 2.

As shown in this Table 2, it is noted that the reaction rate constant of $2SnO_2/2TiO_2$ heterojunction is much higher (i.e., 1.13) compared to those of the other multilayer photocatalysts, and follows the same trend as the photocatalytic degradation performance.

Mechanism discussion

According to the principles of photocatalysis, when a heterojunction photocatalyst receives enough energy, electron–hole pairs are generated in the VB of the semiconductors, and then electron transfers to the CB. In case of $2SnO_2/2TiO_2$ heterojunction (Fig. 11), the electrons excited to the CB of TiO_2 will migrate to the CB of SnO_2 and then reduce the adsorbed $\boldsymbol{O_2}$ to yield $\boldsymbol{O_2^{\cdot -}}$ superoxide radical anions. Similarly, the generated holes in the VB of SnO_2 will migrate to the VB of TiO_2 and then reduce the adsorbed oxidize $\boldsymbol{OH^-}$ radicals to yield $\boldsymbol{OH^{\cdot}}$ radicals. The $\boldsymbol{OH^{\cdot}}$ will react and leads to the dissolution of MB dye. This process can be summarized through the following equations:

$$h\nu \rightarrow (SnO_2/TiO_2) \rightarrow 2(e^- + h^+) + (SnO_2/TiO_2)$$
$$O_2 + e^- \rightarrow O_2^{\cdot -}$$
$$H_2O + O_2^{\cdot -} \rightarrow HO_2^{\cdot} + OH^-$$
$$HO_2^{\cdot} + H_2O \rightarrow H_2O_2 + OH^-$$
$$OH^- + h^+ \rightarrow OH^{\cdot}$$
$$OH^{\cdot} + MB \rightarrow \text{Simpler compounds} + CO_2$$

From the obtained experimental results and the photocatalytic mechanism proposed above, it can be justified that the main factors causing the enhanced degradation of MB dye with varying rate can be associated mainly to the effects of the layer architecture and the ratio of TiO_2 in the heterojunction. It can be clearly noticed that the heterojunction with TiO_2 layers that are in direct contact with the MB dye has higher photocatalytic degradation performance than those of the SnO_2 layers. The SnO_2 layers in direct contact

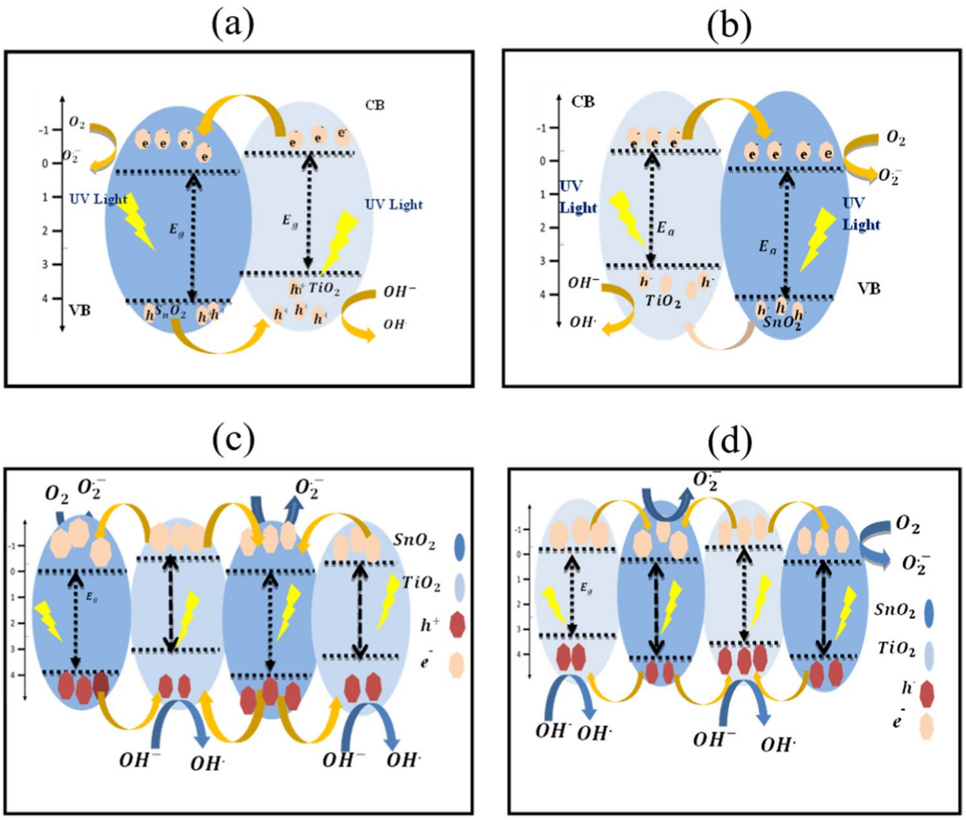

Fig. 11 Mechanism of the MB dye photodegradation by the multilayered films. **a** $2SnO_2/2TiO_2$, **b** $2TiO_2/2SnO_2$, **c** $1SnO_2/1TiO_2$, **d** $1TiO_2/1SnO_2$

with the soda-lime glass substrate prove their effectiveness as a buffering layer and prevent the diffusion of sodium Na to the thin layers, knowing that the Na atoms play a role as recombination centers (Benyakhlef et al. 2020). Furthermore, when the ratio of TiO_2 increases on the surface, the heterojunction photocatalytic efficiency increases. Based on the obtained results provided in Table 1 and Fig. 10, we observed that when the crystallite size of the top thin film increases, the MB degradation rate increases, which is confirmed by several authors (Nandiyanto et al. 2020; Wang et al. 2014). Indeed, the multilayer $2SnO_2/2TiO_2$ can be considered ideal for photocatalytic degradation of organic compounds.

Conclusion

In this study, multilayered TiO_2/SnO_2 films have been successfully fabricated via a simple cost-effective dip coating technique. The films manifest nanocrystalline phases, high adherence, and transparency in the visible light. The films exhibit the anatase TiO_2 and the cassiterite SnO_2 phases. The transparency varies in the range of 75−86%, while the energy band gaps of heterostructures is reduced in comparison to their individual counterparts (i.e., 3.2 for TiO_2, and 3.9 eV for SnO_2) which can potentially perform degradation under visible light. It is found that the TiO_2/SnO_2 multilayer where the SnO_2 is in contact directly with the soda lime glass substrate and the TiO_2 is in contact with the pollutant, demonstrates a high photocatalytic activity than that of the SnO_2/TiO_2 due to the buffer effect of SnO_2 thin layers and the high photodegradation of TiO_2. This study directs the importance of layers' order, the number of layers, and the relative difference of the band gap energy values of the semiconductors.

Acknowledgements The authors would like to thank Prince Sultan University for support.

Author contribution Walid Serbout, Fayçal Bensouici, Omar Meglali, and Sabrina Iaiche: writing—original draft, conceptualization, investigation, data curation, methodology, Mohamed Bououdina, Steffano Bellucci, and Muhammad Humayun: writing—review and editing. resources, funding acquisition.

Data availability The data will be available from the corresponding author on reasonable request.

Declarations

Ethical approval Not applicable.

Consent to participate Not applicable.

Consent to publish Not applicable.

Competing interests The authors declare no competing interests.

References

Abd El-Nasser S, Kim S, Yoon H, Toth R, Pal K, Bechelany M (2020) Sodium-assisted TiO_2 nanotube arrays of novel electrodes for photochemical sensing platform. J Org Electron 76:105443. https://doi.org/10.1016/j.orgel.2019.105443

Abdel-Messih MF, Ahmed MA, El-Sayed AS (2013) Photocatalytic decolorization of Rhodamine B dye using novel mesoporous SnO_2–TiO_2 nano mixed oxides prepared by sol–gel method. J Photochem Photobio A 260:1–8. https://doi.org/10.1016/j.jphotochem.2013.03.011

An L, Wang G, Cheng Y, Zhao L, Gao F, Tian Y (2015) Ultrasonic-assisted synthesis of visible-light-driven TiO_2/Bi_2O_3 nanocomposite photocatalysts: characterization, properties and azo dye removal application. Res Chem Intermed 41:7449–7461. https://doi.org/10.1007/s11164-014-1836-x

Aplin R, Waite TD (2000) Comparison of three advanced oxidation processes for degradation of textile dyes. Water Sci Technol 42(5–6):345–354. https://doi.org/10.2166/wst.2000.0534

Asahi R, Morikawa T, Ohwaki T, Aoki K, Taga Y (2001) Visible-light photocatalysis in nitrogen-doped titanium oxides. Science 293(5528):269–271. https://doi.org/10.1126/science.1061051

Ashkarran AA, Ghavamipour M, Hamidinezhad H, Haddadi H (2015) Enhanced visible light-induced hydrophilicity in sol–gel-derived Ag–TiO_2 hybrid nanolayers. Res Chem Intermed 41:7299–7311. https://doi.org/10.1007/s11164-014-1813-4

Aye T, Anderson WA, Mehrvar M (2003) Photocatalytic treatment of cibacron brilliant yellow 3G-P (reactive yellow 2 textile dye). J Environ Sci Health Part A 38(9):1903–1914. https://doi.org/10.1081/ESE-120022888

Aziz M, Abbas SS, Baharom WRW (2013) Size-controlled synthesis of SnO_2 nanoparticles by sol–gel method. Mater Lett 91:31–34. https://doi.org/10.1016/j.matlet.2012.09.079

Bensouici F, Souier T, Dakhel A, Iratni A, Tala-Ighil R, Bououdina M (2015) Synthesis, characterization and photocatalytic behavior of Ag doped TiO_2 thin film. Superlattices Microstruct 85:255–265. https://doi.org/10.1016/j.spmi.2015.05.028

Bensouici F, Bououdina M, Dakhel A, Tala-Ighil R, Tounane M, Iratni A, Souier T, Liu S, Cai WJASS (2017) Optical, structural and photocatalysis properties of Cu-doped TiO_2 thin films. Appl Surf Sci 395:110–116. https://doi.org/10.1016/j.apsusc.2016.07.034

Benyakhlef M, Bensouici F, Bououdina M, Dakhel A, Tala-Ighil R, Toubane MJ (2020) Surface, structural and optical properties dependence of Fe-doped TiO_2 films deposited onto soda–lime–glass. Surf Interfaces 21:100682. https://doi.org/10.1016/j.surfin.2020.100682

Cheng H-E, Lin C-Y, Hsu C-MJ (2017) Fabrication of SnO_2-TiO_2 core-shell nanopillar-array films for enhanced photocatalytic activity. Appl Surf Sci 396:393–399. https://doi.org/10.1016/j.apsusc.2016.10.166

Chetri P, Basyach P, Choudhury AJ (2014) Exploring the structural and magnetic properties of TiO_2/SnO_2 core/shell nanocomposite: an experimental and density functional study. J Solid State Chem 220:124–131. https://doi.org/10.1016/j.jssc.2014.08.022

Choudhury B, Choudhury AJ (2014) Oxygen defect dependent variation of band gap, Urbach energy and luminescence property of anatase, anatase–rutile mixed phase and of rutile phases of TiO_2 nanoparticles. Physica E Low Dimens Syst Nanostruct 56:364–371. https://doi.org/10.1016/j.physe.2013.10.014

Dai S, Song W, Li T, Zhuang YJ (1996) Study on azo dyes structure–biodegradability relationships. Adv Environ Sci 4:1–9

Dakhel AJ (2010) Electrical and optical properties of iron-doped CdO. Thin Solid Films 518(6):1712–1715. https://doi.org/10.1016/j.tsf.2009.11.026

de Mendonça VR, Lopes OF, Fregonesi RP, Giraldi TR, Ribeiro CJ (2014) TiO_2-SnO_2 heterostructures applied to dye photodegradation: the relationship between variables of synthesis and photocatalytic performance. Appl Surf Sci 298:182–191. https://doi.org/10.1016/j.apsusc.2014.01.157

Derrar K, Zaabat M, Zerrouk I, Hafdallah A, Rouabah N, Gasmi B (2019) Optical and structural properties of SnO_2 thin films deposited by spray pyrolysis technique: effect of solution concentration. Trans Tech Publ 397:179–186. https://doi.org/10.4028/www.scientific.net/DDF.397.179

Dong C, Song H, Zhou Y, Dong C, Shen B, Yang H, Matsuoka M, Xing M, Zhang JJ (2016) Sulfur nanoparticles in situ growth on TiO_2 mesoporous single crystals with enhanced solar light photocatalytic performance. RSC Adv 6(81):77863–77869. https://doi.org/10.1039/C6RA17884G

Farhadi A, Mohammadi M, Ghorbani MJ (2017) On the assessment of photocatalytic activity and charge carrier mechanism of TiO_2@SnO_2 core-shell nanoparticles for water decontamination. J Photochem Photobio A 338:171–177. https://doi.org/10.1016/j.jphotochem.2017.02.009

Ferrere S, Zaban A, Gregg BAJ (1997) Dye sensitization of nanocrystalline tin oxide by perylene derivatives. J Phys Chem B 101(23):4490–4493. https://doi.org/10.1021/jp970683d

Fogler HS (2020) Elements of chemical reaction engineering, 5th edn. Pearson, Boston

Gaya UI, Abdullah AHJ (2008) Heterogeneous photocatalytic degradation of organic contaminants over titanium dioxide: a review of fundamentals, progress and problems. J Photochem Photobio c: Photochem Rev 9(1):1–12. https://doi.org/10.1016/j.jphotochemrev.2007.12.003

Haouanoh D, TalaIghil RZ, Toubane M, Bensouici F, Mokeddem KJMRE (2019) Effects of thermal treatment and layers' number on SnO_2 thin films properties prepared by sol-gel technique. Mater Res Exp 6(8):086422. https://doi.org/10.1088/2053-1591/ab1d96

Hashimoto K, Irie H, Fujishima A (2005) TiO_2 photocatalysis: a historical overview and future prospects. Jpn J Appl Phys 44(12R):8269. https://doi.org/10.1143/JJAP.44.8269

Hoffmann MR, Martin ST, Choi W, Bahnemann DW (1995) Environmental applications of semiconductor photocatalysis. Chem Rev 95(1):69–96. https://doi.org/10.1021/cr00033a004

Idota Y, Kubota T, Matsufuji A, Maekawa Y, Miyasaka T (1997) Tin-based amorphous oxide: a high-capacity lithium-ion-storage material. Science 276(5317):1395–1397. https://doi.org/10.1126/science.276.5317.1395

Irie H, Watanabe Y, Hashimoto KJCL (2003) Carbon-doped anatase TiO_2 powders as a visible-light sensitive photocatalyst. Chem Lett 32(8):772–773. https://doi.org/10.1246/cl.2003.772

Kawahara T, Konishi Y, Tada H, Tohge N, Ito S (2001) Patterned TiO2/SnO2 bilayer type photocatalyst. 2. Efficient dehydrogenation of methanol. Langmuir 17(23):7442–7445. https://doi.org/10.1021/la010307r

Kiruthiga G, Rajni K, Geethanjali N, Raguram T, Nandhakumar E, Senthilkumar N (2022) SnO_2: investigation of optical, structural, and electrical properties of transparent conductive oxide thin films prepared by nebulized spray pyrolysis for photovoltaic applications. Inorg Chem Commun 145:109968. https://doi.org/10.1016/j.inoche.2022.109968

Kusior A, Zych L, Zakrzewska K, Radecka MJ (2019) Photocatalytic activity of TiO_2/SnO_2 nanostructures with controlled dimensionality/complexity. Appl Surf Sci 471:973–985. https://doi.org/10.1016/j.apsusc.2018.11.226

Lin L, Yang Y, Men L, Wang X, He D, Chai Y, Zhao B, Ghoshroy S, Tang QJ (2013) A highly efficient TiO_2@ZnO n–p–n heterojunction nanorod photocatalyst. Nanoscale 5(2):588–593. https://doi.org/10.1039/C2NR33109H

Malik R, Tomer VK, Chaudhary V, Dahiya MS, Rana PS, Nehra S, Duhan SJ (2016) Facile synthesis of hybridized mesoporous Au@TiO_2/SnO_2 as efficient photocatalyst and selective VOC sensor. ChemistrySelect 1(12):3247–3258. https://doi.org/10.1002/slct.201600634

Mathews N, Morales ER, Cortés-Jacome M, Antonio JTJ (2009) TiO_2 thin films–Influence of annealing temperature on structural, optical and photocatalytic properties. Sol Energy 83(9):1499–1508. https://doi.org/10.1016/j.solener.2009.04.008

Meglali O, Attaf N, Bouraiou A, Bougdira J, Aida M, Medjahdi G (2014) Chemical bath composition effect on the properties of electrodeposited $CuInSe_2$ thin films. J Alloys Compd 587:303–307. https://doi.org/10.1016/j.jallcom.2013.10.100

Meglali O, Bouraiou A, Attaf N, Aida MJ (2017) The effect of Al and In concentrations on the properties of electrodeposited Cu(In, Al)Se_2 using two electrode system without the addition of complexing agents. Optik 140:709–717. https://doi.org/10.1016/j.ijleo.2017.04.072

Mehrdad A, Hashemzadeh RJ (2010) Ultrasonic degradation of Rhodamine B in the presence of hydrogen peroxide and some metal oxide. Ultrason Sonochem 17(1):168–172. https://doi.org/10.1016/j.ultsonch.2009.07.003

Minami TJ (2000) New n-type transparent conducting oxides. MRS Bull 25(8):38–44

Mohammadi M, Cordero-Cabrera M, Ghorbani M, Fray D (2006) Synthesis of high surface area nanocrystalline anatase-TiO_2 powders derived from particulate sol-gel route by tailoring processing parameters. J Solgel Sci Technol 40:15–23. https://doi.org/10.1007/s10971-006-8267-0

Nandiyanto ABD, Zaen R, Oktiani R (2020) Correlation between crystallite size and photocatalytic performance of micrometer-sized monoclinic WO_3 particles. Arab J Chem 13(1):1283–1296. https://doi.org/10.1016/j.arabjc.2017.10.010

Norouzi F, Pourmadadi M, Yazdian F, Khoshmaram K, Mohammadnejad J, Sanati MH, Chogan F, Rahdar A, Baino F (2022) PVA-based nanofibers containing chitosan modified with graphene oxide and carbon quantum dot-doped TiO_2 enhance wound healing in a rat model. J Funct Biomater 13(4):300. https://doi.org/10.3390/jfb13040300

Ohno T, Mitsui T, Matsumura MJ (2003) Photocatalytic activity of S-doped TiO_2 photocatalyst under visible light. Chem Lett 32(4):364–365. https://doi.org/10.1246/cl.2003.364

Pal K, Chakroborty S, Panda P, Nath N, Soren SJES (2022) Environmental assessment of wastewater management via hybrid nanocomposite matrix implications—an organized review. Environ Sci Pollut Res 29(51):76626–76643. https://doi.org/10.1007/s11356-022-23122-5

Park N-G, Kang MG, Ryu KS, Kim KM, Chang SHJ (2004) Photovoltaic characteristics of dye-sensitized surface-modified nanocrystalline SnO_2 solar cells. J Photochem Photobiol A 161(2–3):105–110. https://doi.org/10.1016/S1010-6030(03)00280-6

Pérez MH, Peñuela G, Maldonado MI, Malato O, Fernández-Ibáñez P, Oller I, Gernjak W, Malato S (2006) Degradation of pesticides in water using solar advanced oxidation processes. Appl Catal B 64(3):272–281. https://doi.org/10.1016/j.apcatb.2005.11.013

Pourmadadi M, Rajabzadeh-Khosroshahi M, Eshaghi MM, Rahmani E, Motasadizadeh H, Arshad R, Rahdar A, Pandey S (2023) TiO_2-based nanocomposites for cancer diagnosis and therapy: a comprehensive review. J Drug Deliv Sci Technol 82:104370. https://doi.org/10.1016/j.jddst.2023.104370

Qin X, Jing L, Tian G, Qu Y, Feng YJ (2009) Enhanced photocatalytic activity for degrading Rhodamine B solution of commercial Degussa P25 TiO_2 and its mechanisms. J Hazard Mater 172(2–3):1168–1174. https://doi.org/10.1016/j.jhazmat.2009.07.120

Scarisoreanu M, Fleaca C, Morjan I, Niculescu A-M, Luculescu C, Dutu E, Ilie A, Morjan I, Florescu LG, Vasile EJ (2017) High photoactive TiO_2/SnO_2 nanocomposites prepared by laser pyrolysis. Appl Surf Sci 418:491–498. https://doi.org/10.1016/j.apsusc.2016.12.122

Sharma R, Bisen D, Shukla U, Sharma B (2012) X-ray diffraction: a powerful method of characterizing nanomaterials. Recent Res Sci Technol 4(8):77–79

Sofyan N, Ridhova A, Yuwono A, Udhiarto A (2018) Preparation of anatase TiO_2 nanoparticles using low hydrothermal temperature for dye-sensitized solar cell. IOP Conf. Ser.: Mater Sci Eng 316:012055. https://doi.org/10.1088/1757-899X/316/1/012055

Srivastava M, Srivastava A, Goyal A, Mishra A, Tomer P, Dwivedi J, Kishore D (2017) One-pot oxidation of aromatic and cyclic hydrocarbons using the Au (III) and Pd (II) catalyst under microwave irradiation. J Phys Org Chem 30(2):28–31. https://doi.org/10.1002/poc.3602

Wang C-TJ (2007) Photocatalytic activity of nanoparticle gold/iron oxide aerogels for azo dye degradation. J Non Cryst Solids 353(11–12):1126–1133. https://doi.org/10.1016/j.jnoncrysol.2006.12.028

Wang C, Shao C, Zhang X, Liu Y (2009) SnO_2 nanostructures-TiO_2 nanofibers heterostructures: controlled fabrication and high photocatalytic properties. Inorg Chem 48(15):7261–7268. https://doi.org/10.1021/ic9005983

Wang Y, Wang Q, Zhan X, Wang F, Safdar M, He JJ (2013) Visible light driven type II heterostructures and their enhanced photocatalysis properties: a review. Nanoscale 5(18):8326–8339. https://doi.org/10.1039/C3NR01577G

Wang X, Sø L, Su R, Wendt S, Hald P, Mamakhel A, Yang C, Huang Y, Iversen BB, Besenbacher F (2014) The influence of crystallite size and crystallinity of anatase nanoparticles on the photodegradation of phenol. J Catal 310:100–108. https://doi.org/10.1016/j.jcat.2013.04.022

Yoo D, Kim I, Kim S, Hahn CH, Lee C, Cho SJ (2007) Effects of annealing temperature and method on structural and optical properties of TiO_2 films prepared by RF magnetron sputtering at room temperature. Appl Surf Sci 253(8):3888–3892. https://doi.org/10.1016/j.apsusc.2006.08.019

Zakrzewska K, Radecka MJ (2007) TiO_2–SnO_2 system for gas sensing—photodegradation of organic contaminants. Thin Solid Films 515(23):8332–8338. https://doi.org/10.1016/j.tsf.2007.03.019

Zhang D, Gu X, Jing F, Gao F, Zhou J, Ruan SJ (2015) High performance ultraviolet detector based on TiO_2/ZnO heterojunction. J Alloys Compd 618:551–554. https://doi.org/10.1016/j.jallcom.2014.09.004